Optical Engineering

OpticalEngineering.SPIEDigitalLibrary.org

Digital holography experiments with degraded temporal coherence

Douglas E. Thornton
Davin Mao
Mark F. Spencer
Christopher A. Rice
Glen P. Perram

SPIE.

Douglas E. Thornton, Davin Mao, Mark F. Spencer, Christopher A. Rice, Glen P. Perram, "Digital holography experiments with degraded temporal coherence," *Opt. Eng.* **59**(10), 102406 (2020), doi: 10.1117/1.OE.59.10.102406

Digital holography experiments with degraded temporal coherence

Douglas E. Thornton,[a,*] **Davin Mao,**[a] **Mark F. Spencer,**[a,b]
Christopher A. Rice,[a] **and Glen P. Perram**[a]
[a]Air Force Institute of Technology, Department of Engineering Physics,
Wright-Patterson Air Force Base, Ohio, United States
[b]Air Force Research Laboratory, Directed Energy Directorate,
Kirtland Air Force Base, New Mexico, United States

Abstract. To simulate the effects of multiple-longitudinal modes and rapid fluctuations in center frequency, we use sinusoidal phase modulation and linewidth broadening, respectively. These effects allow us to degrade the temporal coherence of our master-oscillator laser, which we then use to conduct digital holography experiments. In turn, our results show that the coherence efficiency decreases quadratically with fringe visibility and that our measurements agree with our models to within 1.8% for sinusoidal phase modulation and 6.9% for linewidth broadening. [DOI: 10.1117/1.OE.59.10.102406]

Keywords: digital holography; coherence.

Paper 191456SS received Oct. 20, 2019; accepted for publication Dec. 18, 2019; published online Jan. 11, 2020.

1 Introduction

Recent results show that digital holography (DH) is an enabling technology for tactical applications, such as deep-turbulence wavefront sensing[1–3] and long-range imaging.[4–6] By flood illuminating a distant object and interfering the scattered signal with a local reference, we can reconstruct the amplitude and phase of the complex-optical field. Furthermore, we can approach the the shot-noise limit, given a strong reference.[7] Recent experiments quantified the validity of this last statement in terms of system efficiencies.[8] While these experiments showed that DH is robust against weak signals often encountered in tactical applications, they assumed the use of fully coherent laser sources when formulating closed-form expressions for the signal-to-noise ratio (SNR).

With coherence in mind, Mandel evaluated the temporal coherence requirements for analog holography in 1966.[9] From this foundational work, Harris et al.[10] studied the role of coherence length in continuous wave (cw) coherent-lidar systems. Recall that coherent lidar uses temporal modulation, whereas DH uses spatial modulation. Because of this difference, cw coherent-lidar systems can operate with ranges many orders of magnitude beyond the coherence length of the master-oscillator (MO) laser.[11–13] In contrast, DH systems cannot, since the hologram interference fringes wash out when the path length differences between the signal and reference are greater than the coherence length of the MO laser.

Claus et al. studied the coherence requirements associated with cw DH systems but with near-equal path lengths between the signal and Ref. 14. In contrast to digital-holographic microscopy, where short laser coherence lengths enable three-dimensional imaging,[15] the effective ranges for tactical applications become limited by both the coherence length and the signal strength. With this last point in mind, Marron et al.[16] successfully conducted field experiments with a DH system using a coherence length >200 m and a range of 100 m. It is unclear, however, whether the path length difference between the signal and reference reduced the fringe visibility,

---

*Address all correspondence to Douglas E. Thornton, E-mail: douglas.thornton@afit.edu

since this detailed information is absent from Ref. 16, in addition to an estimate of the system efficiencies (multiplicative losses), which degrade the achievable SNR.

From our work in Ref. 8, we know that the ideal total-system efficiency becomes limited to about 30%. This limit is primarily due to depolarization from rough surface scattering and the pixel modulation transfer function. Other efficiencies, including those caused by excess reference and signal noise, can further degrade the fringe visibility. On top of these system efficiencies, several independent phenomenon (not studied in Ref. 8) can further degrade the temporal coherence of the MO laser, and subsequently, the fringe visibility of a DH system. For example, increasing the integration time on the focal-plane array (FPA) can reduce the fringe visibility due to fluctuations in the center frequency of the MO laser. High-power laser sources can also exhibit time-evolving longitudinal modes, leading to degraded temporal coherence. In our opinion, these independent phenomena have largely been ignored in previous studies and leads us to the DH experiments presented here.

This paper explores the effects of degraded temporal coherence, given a DH system in the off-axis image plane recording geometry (IPRG). To degrade the temporal coherence of our MO laser, we use two approaches: sinusoidal phase modulation and linewidth broadening. The sinusoidal phase modulation produces spectral side bands and allows us to simulate the effects of multiple-longitudinal modes in our MO laser. Phase modulation via pseudorandom bit sequences (PRBS) then allows us to broaden the linewidth of our MO laser and simulate the effects of rapid fluctuations in the center frequency. Before moving on to the next section, it is worth mentioning that the experimental setup used here may also enable the characterization of high-power fiber lasers, where one might broaden the linewidth of the seed to reduce the effects of stimulated Brillouin scattering.[17,18]

In what follows, we show that the coherence efficiency depends on the square of the complex-degree of coherence (Secs. 2–4). In Sec. 2, we develop the relationship between coherence efficiency and the complex-degree of the coherence, whereas in Sec. 3, we describe our experimental setup and how we measure the coherence efficiency. Section 4 follows with analysis and results of the measured and modeled coherence efficiency. Last, Sec. 5 provides a conclusion for this paper.

2 Coherence Efficiency, η_c

With DH, we interfere the signal with a reference, and we demodulate the resulting digital hologram to obtain an estimate of the amplitude and phase of the complex-optical field. As such, the instantaneous hologram irradiance, i_H, is the square magnitude of the sum of the signal complex-optical field, U_S, and reference complex-optical field, U_R, such that

$$i_H(t,\tau) = |U_R(t)|^2 + |U_S(t+\tau)|^2 + U_R^*(t)U_S(t+\tau) + U_R(t)U_S^*(t+\tau), \tag{1}$$

where t is time, τ is the time delay between the signal and reference, and * denotes complex conjugate. For simplicity in the notation, Eq. (1) neglects any spatial dependencies. Here, we assume that the instantaneous reference irradiance (first term) is spatially uniform and that the instantaneous signal irradiance (second term) is negligible given a strong reference and a weak signal. The third and fourth terms involving U_S have the important spatial content. For example, with the tilted reference provided by an off-axis local oscillator (LO), the third and forth terms of Eq. (1) produce the spatial fringes in i_H and shift these terms away from DC in the spatial Fourier domain of i_H. With these shifts in mind, we window the third term in the spatial Fourier domain and transform back to the spatial domain to obtain an estimate $\hat{U}_S$. The precision of $\hat{U}_S$ depends on the SNR of the DH system.

As with previous works, we use the power definition of the SNR, S/N,[8] such that

$$S/N = \eta_T \frac{4q_I^2}{\pi} \frac{\overline{m}_R \overline{m}_S}{\overline{m}_R + \overline{m}_S}, \tag{2}$$

where η_T is the total-system efficiency, $4q_I/\pi$ is the noise compression factor, and $\overline{m}_R$ and $\overline{m}_S$ are the mean photoelectron count for the reference and signal, respectively. In practice, $\overline{m}_R$ and $\overline{m}_S$ follows as:

$$\overline{m}_R = \frac{t_i p^2}{h\nu} \langle |U_R(t)|^2 \rangle \quad \text{and} \quad \overline{m}_S = \frac{t_i p^2}{h\nu} \langle |U_S(t+\tau)|^2 \rangle, \tag{3}$$

where $t_i p^2/h\nu$ is the irradiance to photoelectron conversion factor (assuming the quantum efficiency is 100%) and $\langle \cdot \rangle$ denotes a time average that is much longer than the temporal period of the MO laser. In the last term of Eq. (2), the numerator is the heterodyne energy and the denominator is the noise energy. With respect to the noise energy, we include only the shot noise associated with the reference and signal and assume other noise sources, such as background noise and FPA read noise, are negligible. Furthermore, η_T contains all the system efficiencies (multiplicative losses) that degrade the fringe visibility, such as optical transmission losses through the atmosphere and receiver optics, the quantum efficiency of the FPA, the mixing efficiency of the signal and reference, etc.[8]

The mixing efficiency is how well the detected reference and signal interfere and thus produce fringes. For example, a phenomenon such as rough-surface scattering from a dielectric object depolarizes the signal and decreases the mixing efficiency by 50%, thus decreasing the visibility of the fringes. A degradation in temporal coherence also leads to a reduction the fringe visibility. Given a cw laser source, the fringe visibility is equivalent to the magnitude of the complex-degree of coherence $\gamma(\tau)$,[19] which we can calculate in terms of U_S and U_R, viz:

$$\gamma(\tau) = \frac{\langle U_S(t+\tau) U_R(t)^* \rangle}{\langle U_S(0) U_R^*(0) \rangle}, \tag{4}$$

where $\langle \cdot \rangle$ represents a time average that is much longer than the temporal period of the laser. The numerator of Eq. (4) represents a cross correlation and the denominator normalizes γ. Thus, the magnitude of γ is a measurable quantity ranging from $\gamma = 1$ (ideal coherence) to $\gamma = 0$ (incoherent).

The heterodyne energy in Eq. (2) assumes ideal coherence between the reference and signal. To quantify the coherence effects in terms of a multiplicative efficiency factor for the total-system efficiency, η_T, we introduce the coherence efficiency, η_c. Since we use a power definition for SNR, S/N, the complex degree of coherence, γ, relates to η_c as

$$\eta_c(\tau) = |\gamma(\tau)|^2. \tag{5}$$

Therefore, the S/N and heterodyne energy is proportional to the square of the fringe visibility. Note that this outcome is the same conclusion as Goodman for the amplitude interferometer.[20] For example, say the MO laser has a Lorentzian spectrum and the time delay, τ, between the reference and signal is equal to the coherence time, τ_c (as defined by Mandel[21]). The MO laser spectrum (i.e., the power spectral density) and γ are Fourier transform pairs via the Wiener–Khinchin theorem;[20] thus, γ is a decaying exponential. This example results in $\gamma = 0.368$, $\eta_c = 13.5\%$, and the DH heterodyne energy and S/N reduces by 86.5%. In terms of the effective range of a practical DH system, the path length difference between the reference and signal, $\Delta\ell$, corresponds to the coherence length, ℓ_c, where $\ell_c = \tau_c c$ and c is the speed of light. Therefore, operating a DH system at $\Delta\ell \geq \ell_c$ is detrimental to the achievable SNR and limits the effective range to $\lesssim \ell_c/2$, assuming the signal travels much further to the object and back as compared to the reference.

3 Experimental Methods

The goal of the experiments presented here was to manipulate the MO laser spectrum with different phase modulation schemes and to quantify the temporal coherence effects by measuring the coherence efficiency, η_c. To that end, we provide the details on the DH experimental setup and the η_c measurements in this section. This work builds upon the results from Ref. 22, which contains additional details.

3.1 *Experimental Setup*

In our experiments, we set up our DH system in the off-axis IPRG as shown in Fig. 1. Here, the MO laser was a Cobalt Samba 1000 cw diode pumped solid state laser with a wavelength of 532.1 nm, a linewidth of <1 MHz, a $\ell_c < 100$ m, and an output power of 1 W. We used

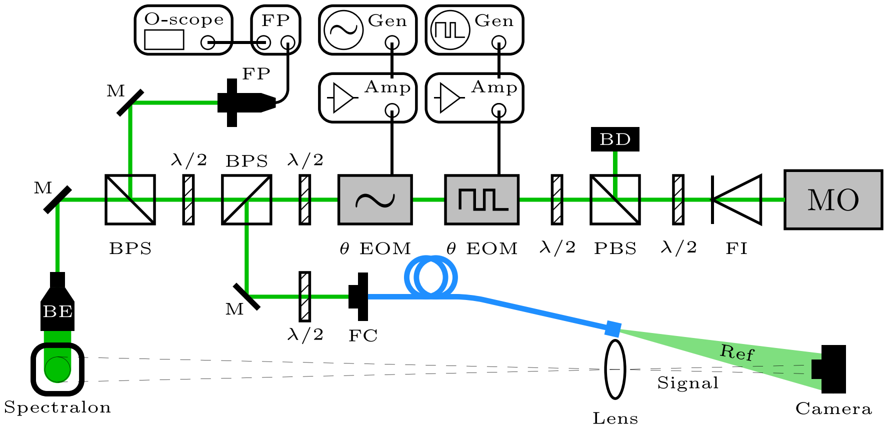

Fig. 1 An overview of the experimental setup.

a Faraday isolator to isolate the MO laser from back reflections. To create the various optical trains found in Fig. 1, we used pairs of half-wave ($\lambda/2$) plates between a polarizing beam splitter to direct (1) unneeded MO laser power to a beam dump, (2) to a fiber coupler for the reference, and (3) to a Fabry–Perot (FP) interferometer. The $\lambda/2$ plates also allowed us to match polarization to the phase electro-optic modulators (θ EOM) and the polarization-maintaining fiber for the reference.

To create the signal, we used a mirror (M) to steer the MO laser into a 20× beam expander to illuminate a sheet of Lapsphere Spectralon. By design, the Spectralon was 99% Lambertian and provided an optically rough dielectric object. After, we imaged the near-Gaussian spot scattered by the Labsphere Spectralon with a 1-in. lens onto a Grasshopper3 camera (GS3-U3-32S4M-C). Here, the object distance and the focal length were 246 and 35 cm, respectively. To create the tilted reference, we placed the off-axis LO next to the lens. Next, we flood illuminated the camera with the tilted reference and collected digital holograms with a camera integration time of 250 μs. This integration time corresponds to a sampling frequency of 4 kHz and is more than three orders of magnitude less than lowest phase-modulation frequency. Therefore, we can safely assume our measurements were not dependent on the integration time.

The first phase EOM was a ConOptics 350-160 with a ConOptics 25D amplifier. We converted it from an amplitude EOM by removing the output polarizer and aligning the laser polarization to one of the EOM crystals' axis. This configuration gave a half-wave voltage, V_π, of 277 V at 532.1 nm. The 25D amplifier was a digital amplifier with a bandwidth from DC to 30 MHz and maximum output voltage of 175 V. To produce linewidth broadening on the MO laser, we used a PRBS input signal with a bit length of 2^{31} and frequencies from 15 to 30 MHz. This broadened the MO laser energy by 62% to 68%.

The second phase EOM was a ConOptics 360-40 with $V_\pi = 155$ V at 532.1 nm. We used a ConOptics 550 amplifier with this EOM, which had a bandwidth of 20 to 500 MHz and maximum output of 125 V peak to peak, V_{pp}. Using a sinusoidal input signal, we generated sidebands on the MO laser with modulation frequencies of 20 to 100 MHz and adjusted the sideband amplitudes by changing the input signal V_{pp}.

To measure the optical spectrum of the phase modulated MO laser, we used a ThorLabs SA30-52 Fabry–Perot interferometer with a finesse of 1500 and free-spectral range (FSR) of 1.5 GHz, which provided a spectral resolution of <1 MHz. The MO laser manufacturer specified linewidth was also <1 MHz. In turn, we scanned the FP mirrors over a range >FSR so that two peaks appeared per scan to convert the recorded FP signal time to relative frequency. We captured multiple scans on the oscilloscope to average the FP output signal and lower the noise. Figure 2 shows the averaged FP spectrum of the unmodulated MO laser spectrum fitted to a Lorentzian lineshape $\mathcal{L}(\nu, \Delta\nu)$ as defined as

$$\mathcal{L}(\nu) = \frac{\pi}{2} \frac{\Delta\nu_L}{(\nu - \nu_0)^2 + \left(\frac{\Delta\nu_L}{2}\right)^2}, \tag{6}$$

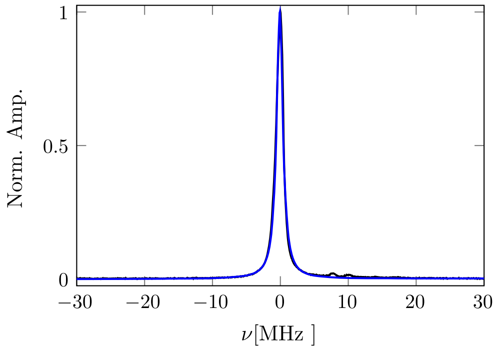

Fig. 2 The average unmodulated MO laser spectrum from the FP interferometer in black with a Lorentzian lineshape fit in blue.

where ν is the MO laser frequency, ν_0 is the center MO laser frequency, $\Delta\nu_L$ is the full width at half max, and A_L is the Lorentzian lineshape amplitude. From Fig. 2, we observed some minor higher-order modes hidden in the noise after averaging, which we assumed to be from the FP alignment and not the MO laser. We chose to fit a Lorentzian lineshape because a high finesse FP interferometer is well approximated by a Lorentzian in lineshape,[23] and we assumed that the MO laser spectrum was near Lorentzian in lineshape.[24] With these assumptions in mind, the observed lineshape was Lorentzian with the linewidth equals to the sum of the FP and MO laser linewidths. The observed unmodulated FHWM was $\Delta\nu_L = 1.2 \pm 0.05$ MHz, which suggests the MO laser linewidth was narrower than specified. The FP manufacturer indicated that the typical best FP linewidth was 700 kHz. With these points in mind, we used $\Delta\nu_L = 500$ kHz for the ensuing analysis with PRBS modulation.

3.2 *Data Measurements*

To measure the coherence efficiency, η_c, for the different phase modulation schemes and path-length differences, we measured the heterodyne energy in the Fourier plane. We maximized the heterodyne energy in the digital hologram by setting the reference at 50% of the pixel full-well depth and increased the signal strength slightly below pixel saturation. To calculate the mean heterodyne energy, $\bar{E}_H$, we performed an inverse discrete Fourier transform ($\mathcal{DFT}^{-1}$) on each hologram and took the magnitude squared to convert the Fourier plane to real-valued energy quantities. Next, we used a mask, $w(x,y)$, to window the total energy, $E_T(x,y)$, contained in the circular pupil in the Fourier plane as shown in Fig. 3; however, this window contained noise in addition to $E_H(x,y)$. To estimate the noise energy, $E_N(x,y)$, we assumed that the Fourier plane was symmetric about the y-axis and used $w(-x,y)$ to window the adjacent quadrant that did not contain a circular pupil (also shown in Fig. 3). Then, we flipped $E_N(x,y)$ and subtracted

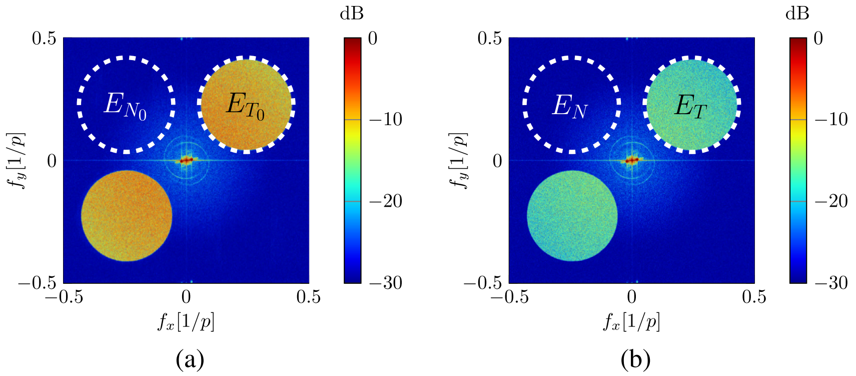

Fig. 3 The Fourier plane of (a) an unmodulated digital hologram and (b) a 20-MHz sinusoidal modulated digital hologram with $\Delta\ell = 3.1$ m. Note that the total energy, E_{T_0} in (a) and E_T in (b), decreases as a result of modulation.

$E_N(-x,y)$ from $E_T(x,y)$ to determine $E_H(x,y)$, which allowed us to perform a pixel-by-pixel average to measure $\bar{E}_H$ for each hologram.

We took measurements at various path length differences between the reference and signal, $\Delta\ell$, by introducing additional lengths of fiber to the reference. Because the strengths of signal and reference were not identical at each $\Delta\ell$, we collected 100 unmodulated digital holograms and 100 modulated digital holograms at the various modulation frequencies at each $\Delta\ell$. We then measured the relative coherence efficiency $\hat{\eta}_c'$, which is the ratio of the modulated $\bar{E}_H$ to the unmodulated $\bar{E}_{H_0}$, viz.

$$\hat{\eta}_c'(\tau) = \frac{\langle \bar{E}_H \rangle}{\langle \bar{E}_{H_0} \rangle} = \frac{\eta_c(\tau)}{\eta_{c_0}(\tau)}, \tag{7}$$

where $\langle\cdot\rangle$ denotes a frame average. Here, $\hat{\eta}_c'$ is the ratio of the modulated η_c to the unmodulated η_{c_0}, since $\bar{E}_N$ is approximately constant across all measurements. Note that this relationship creates a relative measurement because E_{H_0} has a minor η_c loss due to the path length differences.

The unmodulated SNR (i.e., $S/N_0 = \langle \bar{E}_{H_0}/\bar{E}_{N_0} \rangle$) was around 110 to 120, which gave us the desired dynamic range for the measurements. However, we observed some minor reference power loss when the phase EOMs were on. We suspected that this loss was due to a minor change in the beam quality through the EOM crystal, which produced a fiber-coupling loss for the reference. Therefore, we normalized the E_H and E_{H_0} measurements to the mean hologram photoelectron count which countered the minor reference power loss.

4 Analysis and Results

This section presents the analysis and results for the measured relative coherence efficiency, $\hat{\eta}_c'$ [cf. Eq. (7)], with respect to the sinusoidal, PRBS, and combined phase modulation schemes. Sinusoidal phase modulation produced sidebands on the MO laser spectrum, while PRBS phase modulation produced linewidth broadening. Phase modulation, in general, is a nonlinear process with respect to frequency.[25] As such, nonideal hardware performance produced spectra different from expected. In what follows, we first present the FP interferometer measurements, which we used to more accurately represent the actual spectra for our model of $\hat{\eta}_c$, so that we could compare to our measurements of $\hat{\eta}_c'$.

4.1 *Sinusoidal Modulation*

To model the sinusoidal phase modulation, we represented the MO laser complex-optical field $U(t)$ as a Bessel series,[26] such that

$$\begin{aligned} U(t) = U_o J_0(\phi)\cos[2\pi\nu_o t] + U_o \sum_{k=1}^{\infty} J_k(\phi)\{\cos[2\pi(\nu_o + kf_{m,s})] \\ + (-1)^k \cos[2\pi(\nu_o - kf_{m,s})]\}, \end{aligned} \tag{8}$$

where U_o is the unmodulated MO laser amplitude, J_k is the sideband amplitude, ϕ is the depth of phase modulation, ν_0 is the MO laser frequency, and $f_{m,s}$ is the sinusoidal phase modulation frequency. Note that J_k are Bessel coefficients of the first kind and the sum of the squared Bessel coefficients equals 1 to conserve energy. Also note that we assumed monochromaticity with the cosines in Eq. (8). We approximated the sinusoidal phase modulated spectrum, $G_s(\nu)$, as

$$G_s(\nu) = \mathcal{L}(\nu)\{J_0^2(\phi) + \sum_{k=1}^{\infty} J_k^2(\phi)[\delta(\nu_o + kf_{m,s}) + \delta(\nu_o - kf_{m,s})]\}, \tag{9}$$

where $\mathcal{L}(\nu)$ is the Lorentzian MO laser lineshape [cf. Eq. (6)] and $\delta(\nu)$ is the impulse function, which represents the phase modulation-induced sidebands. Here, we assumed that the cross terms are negligible since $\Delta\nu_L \ll f_{m,s}$.

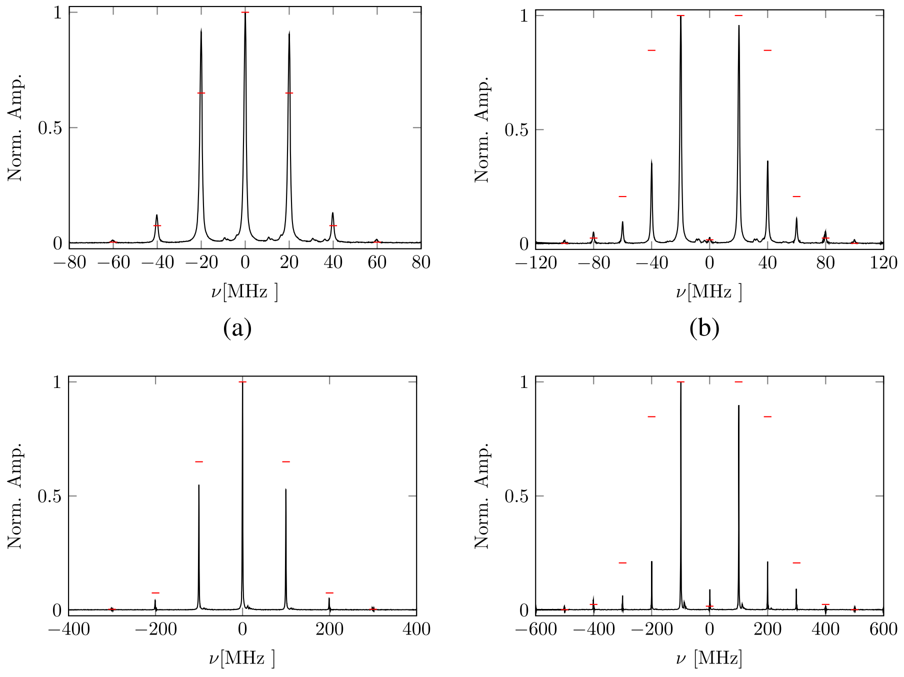

(a) (b) (c) (d)

Fig. 4 The average FP spectra in black of the sinusoidal phase modulated MO laser at $f_{m,s} = 20$ MHz in (a) and (b) and $f_{m,s} = 100$ MHz in (c) and (d) with $\phi = 0.403\pi$ in (a) and (c) and $\phi = 0.806\pi$ in (b) and (d). The theoretical Bessel amplitudes are denoted as (–).

We collected data from $f_{m,s} = 20$ to 100 MHz in five MHz steps at $\phi = 0.4\pi$ and 0.8π. Figure 4 shows a few of the collected FP spectra for the sinusoidal phase modulation. We observed that the sideband amplitudes did not align well with the theoretical Bessel coefficients, were asymmetric, and varied measurably for each $f_{m,s}$ and ϕ. In turn, we calculated the average absolute percent error of the sideband amplitudes, ΔA_k, as

$$\Delta A_k(\phi) = \frac{100}{17} \sum_{f_{m,s}=20\ \mathrm{MHz}}^{100\ \mathrm{MHz}} \frac{1}{2\alpha + 1} \sum_{k=-\alpha}^{\alpha} \frac{|A_k(f_{m,s}, \phi) - J_k^2(\phi)|}{J_k^2(\phi)}, \tag{10}$$

where $f_{m,s}$ ranged from 20 to 100 MHz in 5-MHz increments, α is the number of sidebands included (i.e., $\alpha = 2$ for $\phi = 0.4\pi$ and $\alpha = 4$ for $\phi = 0.8\pi$), and A_k^2 was the FP measured sideband amplitude. These calculations resulted in $\Delta A_k(0.4\pi) = 16\%$ and $\Delta A_k(0.8\pi) = 241\%$. We believe that this discrepancy is due to the nonideal performance of the hardware such as the input sinusoidal signal having some bandwidth, minor differences in the EOM temperature, etc., but not significant FP alignment errors. Therefore, we measured the sideband amplitudes from the FP interferometer to substitute for the Bessel coefficients in the relative coherence efficiency $\hat{\eta}_{c,s}$ model predictions. Each k'th-order sideband had two FP amplitude measurements, so we took the average of the two amplitudes for the corresponding A_k value.

Since $G(\nu)$ and $\gamma(\tau)$ are Fourier transform pairs, the γ_s for the sinusoidal phase modulation resulted in

$$\gamma_s(\tau, \phi, f_{m,s}) = e^{-\pi \Delta\nu \tau} \left[A_0(\phi, f_{m,s}) + 2 \sum_{k=1}^{\infty} A_k(\phi, f_{m,s}) \cos(2\pi k f_{m,s} \tau)\right], \tag{11}$$

where A_k was the sideband amplitude measurements from the FP, the exponential was from the unmodulated MO laser (i.e., the Lorentzian lineshape), and the cosine was the result of the spectral shifts from the sidebands in Eq. (9). Put another way, γ_s was a series of beating cosines resulting from the sidebands with a decaying exponential envelope from the MO laser linewidth.

Note that we normalized the Bessel coefficients in Eq. (8) [i.e., $1 = J_0^2(\phi) + 2\sum_{k=1}^{\infty} J_k^2(\phi)$]. As such, we normalized the measured $A_{k'}s$ in a similar fashion, which also normalizes $\gamma_s(\tau)$, so that the values ranged from zero to one. Since the measured relative coherence efficiency, $\hat{\eta}'_c$, were (by name) relative [cf. Eq. (7)], our model for $\hat{\eta}_{c,s}(\tau)$ (given sinusoidal phase modulation) was

$$\hat{\eta}_{c,s}(\tau, \phi, f_{m,s}) = \left[A_0(\phi, f_{m,s}) + 2\sum_{k=1}^{\infty} A_k(\phi, f_{m,s}) \cos(2\pi k f_{m,s}\tau)\right]^2, \tag{12}$$

where we divided out the exponential from the unmodulated digital hologram by E_{H_0}. Note that $\hat{\eta}_{c,s}$ shows our $\hat{\eta}'_{c,s}$ was solely dependent on the sinusoidal phase modulation and not the unmodulated MO laser linewidth.

Figure 5 shows $\hat{\eta}'_{c,s}$ compared to $\hat{\eta}_{c,s}$ [cf. Eq. (12)] with the FP measured amplitudes (A_k) and the theoretical (J_k). We observed in Figs. 5(a) and 5(b) that $\hat{\eta}'_{c,s}$ approaches 0% when the sidebands destructively interfere and approaches 100% when the sidebands constructively interfere, due to the beating sidebands [cf. Eq. (11)]. As we increased the path length difference between the reference and signal ($\Delta\ell$), the beating sidebands became more apparent, as shown in Fig. 5(c), where $\phi = 0.4\pi$ and $\Delta\ell = 22.4$ m. We took advantage of this sinusoidal structure to better determine the value of τ (i.e., $\tau = \Delta\ell/c$), since we had some uncertainty to the value of τ for Eq. (12). This uncertainty was from the LO fiber optical path length because we did not have the exact refractive index value at the MO laser wavelength. Therefore to estimate τ, we minimized the error between the $\hat{\eta}'_{c,s}$ and $\hat{\eta}_{c,s}$. The results yielded a $\Delta\ell = 3.1$ m for Figs. 5(a) and 5(b) and $\Delta\ell = 22.4$ m, which were within a few centimeters of the measured $\Delta\ell$ when assuming the LO fiber's refractive index ≈1.50. Note that we used these path length difference measurements for the PRBS phase modulation analysis.

Table 1 shows the average absolute difference between $\hat{\eta}'_{c,s}$ and $\hat{\eta}_{c,s}$. We found that our A_k's improved $\hat{\eta}_{c,s} \approx 10\%$ more for $\phi = 0.8\pi$ than for $\phi = 0.4\pi$. This improvement occurred not only because $\Delta A_k(0.4\pi) \ll \Delta A_k(0.8\pi)$, but also because the difference in the energy distribution to the sidebands for each ϕ [cf. Eq. (10)]. For $\phi = 0.4\pi$, $\gtrsim 90\%$ of the energy was contained in the primary ($k = 0$) and first-order ($k = 1$) sidebands for both the theoretical and measured spectrum. For $\phi = 0.8\pi$, $\lesssim 50\%$ of the energy is contained in the first-order sidebands ($k = 1$) for the theoretical spectrum as compared to $\gtrsim 70\%$ of the energy for the measured spectrum. Therefore, the differences in $\Delta A_k(0.8\pi)$ were more sensitive than for $\Delta A_k(0.4\pi)$ and our A_k's provided a much better predictive model for $\hat{\eta}_{c,s}$.

The measurements in Fig. 5 had standard deviations of less than a percent (hence the exclusion from the figures). Our model for $\hat{\eta}_{c,s}$ agreed with our measurements for $\hat{\eta}'_{c,s}$ to within 1.8%, which showed the accuracy of our methodology. In practice, these results show the impracticality of a multilongitudinal mode MO laser. If such a MO laser was used, the SNR would be extremely noisy with moving object in tactical applications due to the beating sidebands and η_c fluctuating, even at ranges within the coherence length ℓ_c.

4.2 *PRBS Modulation*

A change in phase leads to a change in the instantaneous frequency, $\delta\nu$, since

$$\delta\nu = \frac{1}{2\pi}\frac{d\phi}{dt}, \tag{13}$$

where $d\phi/dt$ is the change in phase with respect to time. Equation (13) shows that phase fluctuations in the MO laser phase results in the frequency fluctuations as well. If these phase fluctuations occur on the order or greater than the MO laser linewidth, then the MO laser spectrum will be broadened. Therefore, by imparting deterministic, rapid phase changes in the form of PRBS phase modulation, we partially broadened the MO laser linewidth with a sinc^2 spectral lineshape. We show the spectrum of the MO laser with 15-MHz PRBS phase modulation in Fig. 6. As shown, we did not achieve a fully broadened spectrum because we applied a random discrete phase shift $\Delta\phi \approx 0.6\pi$, whereas previous work used $\Delta\phi \approx \pi$[17] and produced a full sinc^2

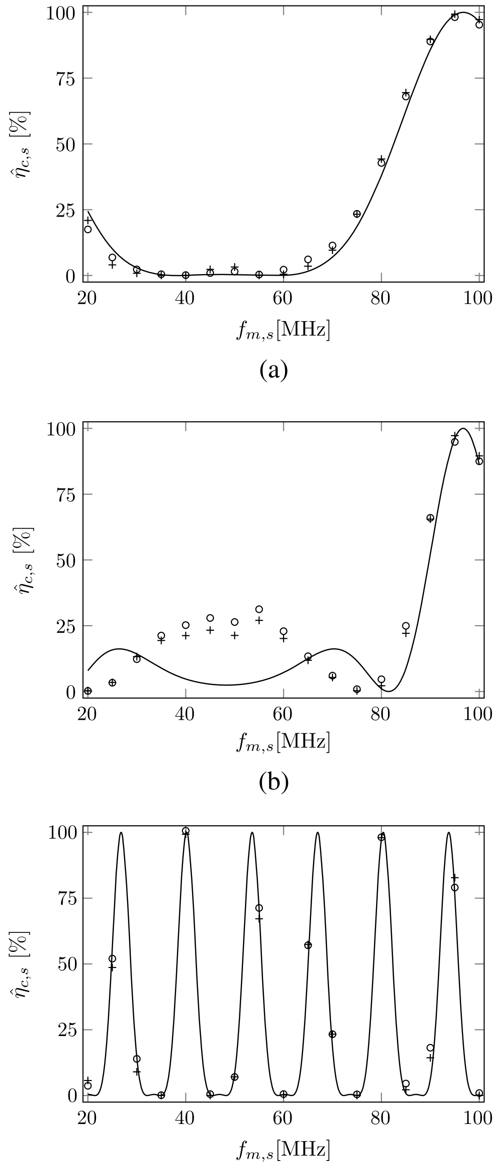

(a)

(b)

(c)

Fig. 5 The measured relative coherence efficiencies, $\hat{\eta}'_{c,s}$, (○) for sinusoidal phase modulation at a depth of modulation of (a and c) $\phi = 0.4\pi$ and (b) $\phi = 0.8\pi$ and at a path length difference of (a and b) $\Delta\ell = 3.1$ m and (c) 22.4 m. These results also show Eq. (12) with the FP measured sideband amplitudes (+) and Eq. (12) with $A_k(\phi, f_{m,s}) = J_k^2(\phi)$ from theory (–).

Table 1 The relative difference between $\hat{\eta}'_{c,s}$ and $\hat{\eta}_{c,s}$ from Fig. 5.

ϕ (rad)	$\Delta\ell$ (m)	$\overline{\lvert\hat{\eta}'_{c,s} - \hat{\eta}_{c,s}\rvert}$	$\overline{\lvert\hat{\eta}'_{c,s} - \hat{\eta}_{c,s}(A_k = J_k^2)\rvert}$
0.4π	3.1	1.5%	2.6%
0.8π	3.1	2.2%	12.1%
0.4π	22.4	1.7%	2.6%

profile. This outcome is much like that observed with the sinusoidal modulation, where increasing ϕ pushed more energy into the sidebands.

Provided Fig. 6, we used a power spectral density, G_p, in the form of a summation of the unmodulated and PRBS modulated spectrums, viz.

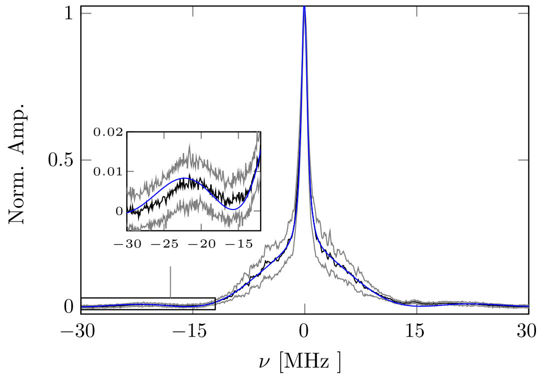

Fig. 6 The average MO laser spectrum with 15-MHz PRBS phase modulation in black, the standard deviation in gray, and the fit with Eq. (14) in blue.

$$G_p(\nu) = \mathcal{L}(\nu) + A_p \operatorname{sinc}^2\left(\frac{\nu - \nu_0}{\Delta\nu_p}\right), \tag{14}$$

where A_p is the sinc^2 amplitude and $\Delta\nu_p$ is the location of the sinc^2 nulls, which are ideally at $f_{m,p}$. We fit Eq. (14) with a baseline to the observed spectra, as shown in Fig. 6 for each $f_{m,p}$. These FP measurements were noisier despite the averaging (cf. the standard deviation of the scans in Fig. 6). We report the important fit results in Table 2, where we rounded the values to the next decimal up from the fit uncertainty (e.g., the fit value = 0.86 with a fit uncertainty of 0.001). To quantify the amount of MO laser energy that was linewidth broadened, we included the factor β, which is the ratio of the sinc^2 area to the total area of the spectrum. We observed that the amount of the linewidth broadening slightly lessened with increasing $f_{m,p}$ and $\Delta\nu_L$ was 100 to 200 kHz less than the measured, unmodulated MO laser linewidth. We assumed this difference in the unmodulated MO laser linewidth was negligible, since it is less than the spectral resolution of the FP (i.e., <1 MHz). From the Fourier transform of Eq. (14), we developed γ_p in the form of

$$\gamma_p(\tau) = (1 - \beta)\exp(-\pi\Delta\nu\tau) + \beta \operatorname{tri}(\tau\Delta\nu_p), \tag{15}$$

where γ_p is a sum of the unmodulated and PRBS modulated $\gamma's$. As such, our model for $\hat{\eta}_{c,p}$ (given PRBS phase modulation) was

$$\hat{\eta}_{c,p}(\tau) = [(1 - \beta) + \beta \operatorname{tri}(\tau\Delta\nu_p)\exp(\pi\Delta\nu_L\tau)]^2, \tag{16}$$

where tri is the triangle function. We assumed $\Delta\nu_L = 500$ kHz, which is consistent with the FP manufacturer specification for the typical best spectral resolution of <700 kHz. In addition, we also assumed $\Delta\nu_L$ is the same for the unmodulated and modulated measurements despite the minor differences between the FP fits.

We measured $\hat{\eta}'_{c,p}$ at four different optical path length differences $\Delta\ell = 3.1$, 7.5, 14.9, and 22.4 m, which we estimated using the same technique as before for the sinusoidal phase modulation. Figure 7 show these results. The measurements were noisier than the sinusoidal phase

Table 2 Fit results of Eq. (14) with the MO laser spectrums resulting from PRBS phase modulation.

f_m (MHz)	A_L	$\Delta\nu_L$ (MHz)	A_p	$\Delta\nu_p$ (MHz)	β
15	0.86	1.0	0.18	15.6	0.68
20	0.85	1.1	0.13	20.9	0.64
25	0.90	1.1	0.11	25.6	0.64
30	0.92	1.1	0.09	30.6	0.62

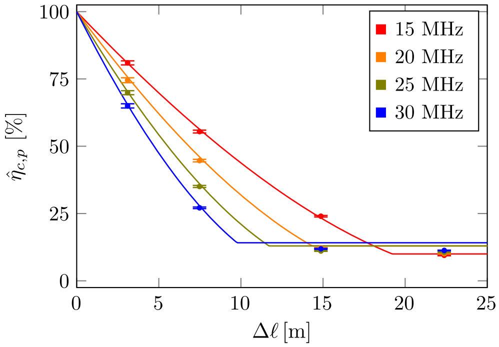

Fig. 7 PRBS phase modulation results at various optical path length differences ($\Delta\ell$). The points represent the mean measured relative coherence efficiency, $\hat{\eta}'_{c,p}$, with PRBS phase modulation, the error bars represent minimum and maximum measurement, and the lines represent Eq. (16) from the FP fits.

modulation measurements. However, the trends in the $\hat{\eta}'_{c,p}$ agreed well with $\hat{\eta}_{c,p}$ and the spectral measurements. The tri function in Eq. (16) well represented the slopes of the lines, where the average absolute error was 1.4%. Each $f_{m,p}$ leveled out at $\approx(1-\beta)^2$, which is beyond the PRBS phase modulation coherence length, and that level increased slightly with $f_{m,p}$, which we saw in the FP spectrum measurements. The $\hat{\eta}'_{c,p}$ data points showed that β was slightly greater than the FP measured value because the data points fell below the line. However, the extrapolated β values from the data points using Eq. (15) were within a few percent of the FP measured values. These differences led to an average absolute error of 6.9%, which was higher than the sinusoidal phase modulation.

This PRBS phase modulation with a $\Delta\phi \approx 0.6\pi$ at 15 to 30 MHz was representative of rapid frequency fluctuations. Effectively, this effect broadened the MO laser spectrum and shortened ℓ_c, since our t_i captured the digital hologram over many phase fluctuation (i.e., $t_i > 1/f_{m,p}$). Therefore, rapid phase fluctuations would decrease ℓ_c and the effective range of a practical DH system.

4.3 *Sinusoidal with PRBS Modulation*

Lastly, we took measurements for $\hat{\eta}'_{c,sp}$ with sinusoidal phase modulation at $f_{m,s} = 20$ to 100 MHz combined with PRBS phase modulation at $f_{m,p} = 30$ MHz. We initially expected the two phase modulation effects to decrease $\hat{\eta}'_{c,sp}$ more than the product of $\hat{\eta}'_{c,s}$ and $\hat{\eta}'_{c,p}$ for low $f_{m,s}$, where the wings of the PRBS spectrum overlaps the sinusoidal phase modulation sidebands. Then as $f_{m,s}$ increased, $\hat{\eta}'_{c,sp} \approx \hat{\eta}'_{c,s}\hat{\eta}'_{c,p}$. However, we show in Fig. 8 that we decently approximated the resulting spectrum by substituting $G_p(\nu)$ for $\mathcal{L}(\nu)$ in Eq. (9) at $f_{m,s} = 20$ MHz and that this approximation becomes better as $f_{m,s}$ increased. We believe that the small amplitude difference in the broad pedestal between the two lines at $f_{m,s} = 20$ MHz was due to the

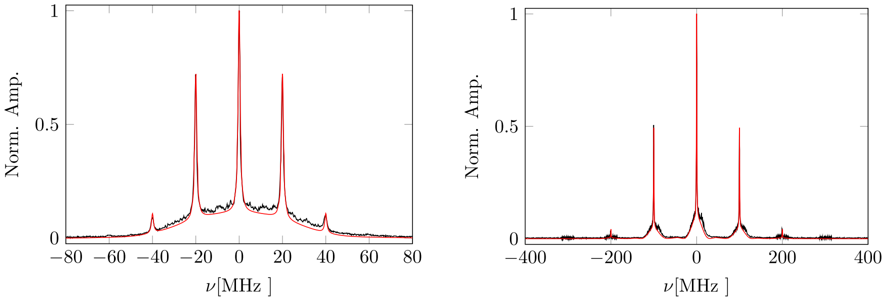

(a) (b)

Fig. 8 The average MO laser spectrum in black with PRBS $f_{m,p} = 30$ MHz and sinusoidal phase modulation with $\phi = 0.4\pi$ and $f_{m,s} = 20$ MHz (a) and 100 MHz (b). Also shown, Eq. (9) with $G_p(\nu)$ substituted for the Lorentzian lineshape in red.

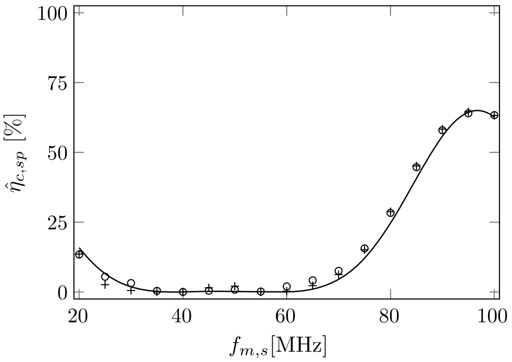

Fig. 9 The mean measured relative coherence efficiency, $\hat{\eta}'_{c,sp}$, with the combination of PRBS phase modulation $f_{m,p} = 30$ MHz and sinusoidal phase modulation with $\phi = 0.4\pi$ and $f_{m,s} =$ 20–100 MHz (○). Also shown, the product of $\hat{\eta}'_{c,s}$ from Fig. 5(a) and $\hat{\eta}'_{c,p}$ for $f_{m,p} = 30$ MHz (+), and Eq. (12) with $A_k = J_k^2$ multiplied by Eq. (16) for $\Delta\nu_p = f_{m,p} = 30$ MHz (–).

exclusion of the cross terms in Eq. (9). Otherwise, we observed no correlation was observed between the two modulation types, and the MO laser spectrums aligned well with our expectations from the previous FP measurements.

Figure 9 shows the results of $\hat{\eta}'_{c,sp}$ at $\Delta\ell = 3.1$ m. The product of $\hat{\eta}_{c,s}$ and $\hat{\eta}_{c,p}$ aligned well with $\hat{\eta}'_{c,sp}$, since the average absolute difference was 0.9%. Altogether, this outcome shows that the efficiency losses associated with multiple coherence effects are multiplicative when there is no correlation between the coherence effects.

5 Conclusion

In this paper, we quantified different coherence effects on the heterodyne energy for DH in terms of a coherence efficiency, η_c. We showed the quadratic relationship between the magnitude of the complex degree of coherence γ and η_c. Then, we experimentally measured the heterodyne energy losses using sinusoidal and PRBS phase modulation to change the coherence properties of the single-mode MO laser. The sinusoidal phase modulation produced sidebands on the MO laser's center frequency, which is representative of the multilongitudinal mode laser. The results show the impracticality of a multilongitudinal mode laser for a DH system, because the SNR will fluctuate rapidly with a moving object in tactical applications. The PRBS phase modulation produced a partially broaden spectrum, which is representative of rapid fluctuations of the MO laser's frequency. For both modulation types, the measurements agreed well with the predictions, provided separate measurements from an FP, with an average absolute error of 1.8% for sinusoidal phase modulation and 6.8% for PRBS phase modulation. Such rapid phase fluctuations decreases the coherence length ℓ_c and thus the effective range of a DH system in practice.

We also combined the sinusoidal and PRBS phase modulation to investigate the total effect of two independent coherence effects. We observed no correlation between the two phase modulation types, and we approximated the measurements as the multiplication of the two independent coherence effects with an average absolute error of 0.9%. These results also show that DH is an effective technique to measure laser coherence effects.

Acknowledgments

The authors declare that there are no conflicts of interest related to this article.

References

1. M. F. Spencer et al., "Deep-turbulence wavefront sensing using digital-holographic detection in the off-axis image plane recording geometry," *Opt. Eng.* **56**(3), 031213 (2016).

2. M. T. Banet, M. F. Spencer, and R. A. Raynor, "Digital-holographic detection in the off-axis pupil plane recording geometry for deep-turbulence wavefront sensing," *Appl. Opt.* **57**(3), 465–475 (2018).
3. D. E. Thornton, M. F. Spencer, and G. P. Perram, "Deep-turbulence wavefront sensing using digital holography in the on-axis phase shifting recording geometry with comparisons to the self-referencing interferometer," *Appl. Opt.* **58**(5), A179–A189 (2019).
4. C. J. Pellizzari, M. F. Spencer, and C. A. Bouman, "Phase-error estimation and image reconstruction from digital-holography data using a Bayesian framework," *J. Opt. Soc. Am. A* **34**(9), 1659–1669 (2017).
5. C. J. Pellizzari et al., "Demonstration of single-shot digital holography using a Bayesian framework," *J. Opt. Soc. Am. A* **35**, 103–107 (2018).
6. C. J. Pellizzari, M. F. Spencer, and C. A. Bouman, "Imaging through distributed-volume aberrations using single-shot digital holography," *J. Opt. Soc. Am. A* **36**(2), A20–A33 (2019).
7. M. F. Spencer, "Spatial heterodyne," in *Encyclopedia of Modern Optics II*, B. Guenther and D. Steel, Eds., Vol. IV, pp. 369–400, Elsevier, Cambridge, Massachusetts (2018).
8. D. E. Thornton et al., "Digital holography efficiency measurements with excess noise," *Appl. Opt.* **58**(34), G19–G30 (2019).
9. L. Mandel, "Wavefront reconstruction with light of finite coherence length," *J. Opt. Soc. Am.* **56**, 1636_1–1637 (1966).
10. M. Harris et al., "The role of laser coherence length in continuous-wave coherent laser radar," *J. Mod. Opt.* **45**(8), 1567–1581 (1998).
11. E. Fischer, E. Dalhoff, and H. Tiziani, "Overcoming coherence length limitation in two wavelength interferometry: an experimental verification," *Opt. Commun.* **123**, 465–472 (1996).
12. U. Hofbauer, E. Dalhoff, and H. Tiziani, "Double-heterodyne-interferometry with delay-lines larger than coherence length of the laser light used," *Opt. Commun.* **162**, 112–120 (1999).
13. Y. Salvadé et al., "Interferometric measurements beyond the coherence length of the laser source," *Opt. Express* **24**(19), 21729–21743 (2016).
14. D. Claus, D. Iliescu, and J. M. Rodenburg, "Coherence requirement in digital holography," *Appl. Opt.* **52**(1), A326–A335 (2013).
15. G. Pedrini and H. J. Tiziani, "Short-coherence digital microscopy by use of a lensless holographic imaging system," *Appl. Opt.* **41**(22), 4489–4496 (2002).
16. J. C. Marron et al., "Atmospheric turbulence correction using digital holographic detection: experimental results," *Opt. Express* **17**(14), 11638–11651 (2009).
17. B. Anderson et al., "Comparison of phase modulation schemes for coherently combined fiber amplifiers," *Opt. Express* **23**(21), 27046–27060 (2015).
18. B. M. Anderson, A. Flores, and I. Dajani, "Filtered pseudo random modulated fiber amplifier with enhanced coherence and nonlinear suppression," *Opt. Express* **25**(15), 17671–17682 (2017).
19. E. Wolf, *Theory of Coherence and Polarization of Light*, Cambridge University Press, Cambridge (2007).
20. J. W. Goodman, *Statistical Optics*, 2nd ed., Wiley, New York (2015).
21. L. Mandel, "Fluctuations of photon beams: the distribution of the photo-electrons," *Proc. Phys. Soc.* **74**(3), 233–243 (1959).
22. D. Mao et al., "Effects of sinusoidal phase modulation on the signal-to-noise ratio in a digital holography system," *Proc. SPIE* **11135**, 111350E (2019).
23. N. Ismail et al., "Fabry–Pérot resonator: spectral line shapes, generic and related Airy distributions, linewidths, finesses, and performance at low or frequency-dependent reflectivity," *Opt. Express* **24**(15), 16366–16389 (2016).
24. J. Buus, M.-C. Amann, and D. J. Blumenthal, *Tunable Laser Diodes and Related Optical Sources*, 2nd ed., SPIE Press, Bellingham, Washington (2005).
25. J. D. Gaskill, *Linear Systems, Fourier Transforms, and Optics*, Wiley, New York (1978).
26. P. E. Powers, *Field Guide to Nonlinear Optics*, SPIE Press, Bellingham, Washington (2013).

Biographies of the authors are not available.